A highly efficient supported TiO$_2$ photocatalyst for wastewater remediation in continuous flow

Oscar Cabezuelo [1], Luis N. Ponce-Gonzalez [1], M. Luisa Marin [*], Francisco Bosca [*]

Instituto de Tecnología Química, Universitat Politècnica de València-Consejo Superior de Investigaciones Científicas, Avda. de los Naranjos s/n, E-46022, Valencia, Spain

A B S T R A C T

Although TiO$_2$ materials have been extensively studied as photocatalysts, there is not any commercial TiO$_2$-supported photocatalyst used for wastewater remediation. This fact set the goal to synthesize a new supported titanium dioxide photocatalyst which, besides being robust, also has a high reaction surface and a very efficient TiO$_2$ shell thickness. Hence, we present a novel TiO$_2$-supported photocatalyst composed of titania-covered glass wool (GW) fibers decorated with SiO$_2$@TiO$_2$ core-shell spheres. For optimizing the photocatalytic activity of this material, the surface of SiO$_2$ microspheres, as well as, the highly mechanically resistant GW fibers, were covered by a robust titania layer of ca. 20–30 nm of thickness. This layer contains nanometric crystals, ca. 12 nm in size, linked to each other and to the surfaces of both SiO$_2$ microspheres and GW. An exhaustive characterization of the physicochemical properties of this new SiO$_2$-TiO$_2$ composite was performed to confirm the Si—O—Ti linkage and the anatase crystal phase. The photocatalytic activity was initially evaluated in batch through the photo-degradation of Methylene Blue as a standard dye. Afterward, the addition of the new photocatalyst in a *solid phase stationary* (SPS) photoreactor coupled to a TOC detector allowed studying *in situ* the mineralization of the recalcitrant pollutant phenol under a continuous flow regime. Results revealed that the optimized TiO$_2$ surface of the SiO$_2$-TiO$_2$ composite produced the complete mineralization of phenol in less than three minutes. Even more, it was demonstrated that this photocatalyst is suitable for the industrial scale-up of wastewater treatment because it does not leach titania, its reuse does not require filtration procedures, and it can be easily implemented in SPS photoreactors at plant scale. In this context, the new material could be a good starting point to prepare other supported photocatalysts for wastewater remediation.

1. Introduction

Conventional wastewater treatment methods such as bacteriological digestion, chlorination, or ozonization have demonstrated to be insufficient to eliminate biologically toxic POPs and CECs and can produce further disinfection byproducts (e.g. halogenated compounds) [1]. As legislation will tighten up towards stricter environmental policies, more efficient methods must be developed to mineralize POPs and CECs. To this aim, Advanced Oxidation Processes (AOPs) are a promising alternative that relies on the formation of highly reactive species to transform recalcitrant organic pollutants into biodegradable compounds or even mineralize them into carbon dioxide and water [2].

Among different AOPs, heterogeneous photocatalysis based on semiconductors has been reported as a viable option for wastewater remediation [3–7]. In this sense, titanium dioxide (TiO$_2$) is a widely recognized photocatalyst with demonstrated efficiency in the removal of organic pollutants based on the photogenerated hydroxyl radical (·OH). Moreover, its high resistance to photo-corrosion and its capability to use natural solar radiation have converted TiO$_2$ into the most used photocatalyst for wastewater treatment over other semiconductors [8–10]. However, this photocatalyst shows some downsides that limit straightforward applications to large-scale industrial processes. For instance, the use of commercial TiO$_2$ (e.g., P25) as a suspension in slurry photoreactors involves the setting of turbulent flow regimes to avoid clogging in continuous working conditions and loss of photoactive area due to particle aggregation [11]. In addition, costly filtration procedures are needed to reutilize the photocatalyst and isolate the treated water, which might contain leached titania [12].

Those problems have partially been solved using a *solid phase stationary* (SPS) photoreactor where the photocatalytic TiO$_2$ powder is

immobilized onto a fixed transparent surface, such as the reactor wall or a fiber mesh [13,14]. However, the reaction rate is usually limited by the pollutant mass transport from the mobile phase to the photocatalyst surface. Hence, there is a need for a reactor whose design provides close contact between the pollutant and the photocatalyst surface, together with a high ratio of the illuminated immobilized photocatalyst [15]. Moreover, to maximize the TiO$_2$ photoreactivity, it is also crucial to consider the optimum TiO$_2$ thickness in the supported photocatalysts [16–20]. In this regard, a previous deep study about the optimum TiO$_2$ thickness for photocatalytic SiO$_2$-TiO$_2$ core@shell materials, proves that thickness values between 20 and 30 nm are the best [21]. Even more, these materials constitute promising alternatives to settle several of the limitations of TiO$_2$ as a photocatalyst. Thus, nanosized TiO$_2$ is grown as a *shell* on the surface of a specific *core* material, preventing the nanosized particle agglomeration and improving the recovery from the media [20, 22]. It is known that core@shell systems allow the customization of materials by modulating the thickness of the shell and the size of the core [16,23]. However, the synthetic methods employed do not ensure partial leaching of TiO$_2$ upon photoreaction [24–26]. Despite the significant improvement that core@shell technology represents compared to nanosized TiO$_2$, several problems remain in large-scale photoreactor design. In this sense, uniform distribution of the photocatalyst in the photoreactor, partial leaching, and separation processes to recycle the photocatalyst make practical applications still costly, operationally complicated, time-consuming, and expensive [13,27,28].

Assemblies of TiO$_2$ nanoparticles/nanostructures into macroscopic architectures have also been extensively studied to create photocatalysts with high photocatalytic activity and easy separation [29,30,14]. However, the photoactive TiO$_2$ thickness was not considered to optimize the photocatalytic efficiency of the materials. In this context, TiO$_2$ fibers with diameters ranging from nano to microscale were fabricated by versatile electrospinning techniques, but in these cases, their polycrystalline nature causes poor mechanical strength, seriously restricting their applications for industrial wastewater treatment [31–33].

In this framework, phenol (P) is the main organic constituent found in effluents of coal conversion processes, coke ovens, petroleum refineries, phenolic resin, herbicide, or fiberglass manufacturing, and petrochemicals [34–36], becoming the major source of industrial water pollution [37]. Moreover, phenol has been designated as a priority pollutant by the US Environmental Protection Agency (EPA) and the National Pollutant Release Inventory (NPRI) of Canada due to its hazardous health effects, acute and chronic, ranging from kidney and nervous system issues to coma and arrests respiratory effects for long exposures [38,39]. In the past decades, conventional wastewater treatment technologies have been established for the removal of phenol from industrial effluents. For instance, adsorption, chemical oxidation, extraction, ozonation, distillation, and electrochemical treatments [40–42]. However, these technologies have intrinsic undesired features, such as low efficiency, high cost, incompleteness of purification, and formation of harmful by-products [43].

With this background, the present work aims to design and develop a novel, recyclable, and robust heterogeneous photocatalyst based on TiO$_2$ with an optimum photoactive TiO$_2$ thickness and a high reaction surface to be implemented into a flow system for continuous photocatalytic wastewater remediation.

First, to overcome the limitations of nanosized TiO$_2$, this photocatalyst will be incorporated into a macroscopic heterogeneous support. Over different available macroscopic supports, we will select commercial glass wool (GW) fibers since they possess excellent chemical/thermal stability, high flexibility, and optical transparency in the UV absorption region of titanium dioxide [44,45]. Besides, to increase the TiO$_2$ surface of the supported photocatalyst, GW microfibers will be decorated with SiO$_2$@TiO$_2$ microspheres. A modified sol–gel synthesis will guarantee the optimum thickness of TiO$_2$, and the absence of leaching in the final photocatalyst.

After extensive characterization of the novel supported photocatalyst, its photocatalytic efficiency will be evaluated in the mineralization of phenol using a homemade continuous flow *solid phase stationary* (SPS) photoreactor at a lab scale.

2. Materials and methods

2.1. Chemicals

Tetraethyl orthosilicate 98 % (TEOS), ammonium hydroxide 28–30 %, absolute ethanol, titanium (IV) isopropoxide 97 % (TTIP), 2-propanol 99.5 %, glass wool (GW, diameter of fiber of 15–25 μm), phenol 99 % and methylene blue 82 % (MB) were purchased from Sigma-Aldrich. Hydrochloric acid 37 % was purchased from Fisher Scientific.

2.2. Instrumentation

Transmission electron microscopy (TEM) and High-Resolution TEM (HRTEM) analyses were carried out through a JEM 2100F transmission electron microscope operated at an accelerating voltage of 200 kV. The samples were deposited as a solid dispersion on a copper grid.

The synthesized materials were analyzed on an ULTRA 55 FESEM at an accelerating voltage of 1.00 kV. Samples were prepared as solid dispersions on carbon tape.

The TiO$_2$ shell of the SiO$_2$-TiO$_2$ composite was trenched and analyzed on an AURIGA C Focused Ion Beam (FIB) at an electron beam accelerating voltage of 1.00 kV with a Gallium ion gun. Samples were prepared as a solid dispersion over carbon tape.

The specific surface area (SSA) was estimated from nitrogen adsorption isotherms through the Brunauer–Emmet–Teller (BET) method using an ASAP2420 BET-Surface area equipment from Micrometrics Ltd at 77 K.

The X-ray diffractograms of powder samples of SiO$_2$ and composites were carried out at a scan rate of 0.5° min^{-1} with a CUBIX XRD DY0822 X-ray radioactive system from PANalytical Ltd. operated at 30 mA and 40 kV using Ni-filtered Cu Kα X-ray radiation ($\lambda = 1.540$ Å) to determine the crystal phase.

Raman spectra were recorded at ambient temperature with a 785 nm HPNIR excitation laser on a Renishaw via Reflex Raman spectrometer equipped with an Olympus microscope and a CCD detector. The laser power on the sample was 15 mW and a total of 20 acquisitions were taken for each spectrum.

Diffuse reflectance spectra were recorded using a Cary-5000 UV–vis spectrophotometer from Variant Factory Ltd.

X-ray photoelectron spectroscopy (XPS) analysis was performed using a SPECS spectrometer equipped with a Phoibos 150 MCD-9 detector using monochromatic Al Kα (1486.6 eV) X-ray radiation. The pass energy was 30 eV, and the X-ray power was 100 W. Spectra treatment was performed using CASA software. Binding energies (BE) were referenced to adventitious carbon (C1s at 284.5 eV).

The TiO$_2$ loading on the SiO$_2$@TiO$_2$ spheres and on the SiO$_2$-TiO$_2$ composite was determined by inductively coupled plasma optical emission spectrometry (ICP-OES) using a Varian 715-ES spectrometer. The new materials were nd disaggregated in a 40 % HF solution for 90 min at 200 °C in an ETHOS1 microwave from Milestone.

The employed radiometer was a P-2110, Gigahertz-Optik with radiometric detector head RW-3705-5.

UV–vis spectra were recorded using a Varian Cary 50 UV–vis spectrophotometer from Agilent Technologies.

The employed UPLC was a Waters Acquity UPLC System with 2996 PDA Detector, Sample Manager, and Binary Solvent Manager from Waters.

Total Organic Carbon analysis was performed with a 450TOC Mettler-Toledo Thornton.

Chronoamperometry curves were performed using a Gamry Instruments potentiostat.

2.3. Synthesis of the SiO₂-TiO₂ composite

First, the silica spheres were prepared according to the Stöber method in basic media [46]. Briefly, TEOS (60.3 mL) was added to a solution of NH_4OH 28–30 % (262 mL) in EtOH (1500 mL) at 0 °C. After 2 h stirring at 0 °C, the reaction was conducted at room temperature for a further 24 h. Afterward, the obtained SiO_2 spheres were centrifuged (4000 rpm for 5 min), washed with EtOH (3 × 300 mL), and dried under vacuum to obtain 10 g of SiO_2 spheres (61.2 % yield) as a white powder.

Then, the synthesized SiO_2 (10 g) was sonicated in EtOH (900 mL) until complete dispersion (*ca.* 1 h) and then heated up to 75 °C. Next, a solution of TTIP (10 mL) in 2-propanol (82 mL) was added dropwise to the SiO_2 suspension. Afterward, the reaction mixture was conducted for a further 20 h at 75 °C under a humidified airflow of 1.5 L min⁻¹. Then, it was cooled to room temperature, and the synthesized $SiO_2@TiO_2$ spheres were centrifuged (4000 rpm for 20 min), washed with EtOH (3 × 150 mL) and water (3 × 150 mL), dried under vacuum, and then calcined at 500 °C for 2 h (room temperature to 500 at 10 °C min⁻¹). The $SiO_2@TiO_2$ spheres (11.1 g with a reaction yield of 87.8 %) were obtained as a white powder.

In parallel, glass wool (GW, 30 g) was smoothly stirred in HCl 6 M (1000 mL) for 12 h. Then, the GW was rinsed with distilled water until pH 6, prior to immersing it in NH_4OH 1 M (500 mL), and subsequently rinsed with distilled water until pH 10. Finally, the GW was washed with EtOH (3 × 250 mL) and then dried at 100 °C for 24 h.

This washed GW was submitted to two consecutive TiO₂ coating + $SiO_2@TiO_2$ sphere decoration procedures. The employed methodology is as follows:

Washed GW (25.4 g) was suspended in EtOH (1000 mL) and heated to 75 °C prior to the addition of a TTIP (0.6 mL) solution in 2-propanol (16 mL) under vigorous stirring. After 2 h at 75 °C, the reaction was conducted for a further 20 h at this temperature under a humidified airflow of 1.5 L min⁻¹. Then, a suspension of the previously synthesized $SiO_2@TiO_2$ spheres (1.2 g) in EtOH (500 mL) was added to the reaction mixture, and it was kept at a 75 °C under vigorous stirring under a humidified airflow of 1.5 L min⁻¹ for a further 20 h. Then, the resulting material was filtered and washed with H_2O (150 mL) and EtOH (250 mL) and dried at 100 °C overnight prior to calcination at 500 °C for 2 h (room temperature to 500 at 10 °C min⁻¹).

The just synthesized material (24.2 g) was submitted to a second consecutive TiO₂ coating, $SiO_2@TiO_2$ spheres decoration, and calcination procedure to obtain the final SiO_2-TiO₂ composite.

2.4. Analysis of the adsorption-desorption capacity of the SiO₂-TiO₂ composite

The adsorption of MB on the SiO_2-TiO₂ composite surface was evaluated according to the following procedure: a suspension (17.5 mg mL⁻¹, 70 mg) of the SiO_2-TiO₂ composite in an aqueous solution of MB (1.5×10^{-5} M, 4 mL) was kept in absence of light for 2 h at 25 °C. Aliquots from the mixture were filtered with a CLARIFY-PTFE 13 mm syringe filter with 0.22 μm porous, and their absorbance was recorded in the UV–vis spectrophotometer after 30 min, 60 min, and 120 min. The spectrum of an aqueous solution of MB (1.5×10^{-5} M) was employed as a reference.

The desorption of MB from the material was evaluated using ethanol as a desorbing solvent. Thus, after 2 h in darkness, the SiO_2-TiO₂ composite was removed from the reaction mixture and washed with ethanol for 1 h (2 × 4 mL). Then, the ethanolic solution was filtered with a CLARIFY-PTFE 13 mm syringe filter with 0.22 μm porous, and its absorbance was recorded in the UV–vis spectrophotometer.

The adsorption of P on the SiO_2-TiO₂ composite was studied using the same procedure as described for MB. For this aim, a suspension of the SiO_2-TiO₂ composite (17.5 mg mL⁻¹, 70 mg) in an aqueous solution of P (10^{-5} M, 4 mL) was kept in darkness for 2 h at 25 °C. In this case, the aliquots were monitored both using the UV–vis spectrophotometer and a

UPLC with a tunable UV detector. Thus, UPLC analysis was carried out with an ACQUITY UPLC BEH C18 1.7 μm column. The mobile phase was fixed at 0.5 mL min⁻¹ with an isocratic mixture of 70 % water (1 % formic acid) and 30 % acetonitrile. Aliquots of 5 μL were injected, and the detection wavelength range was selected from 210 nm to 400 nm.

2.5. Evaluation of the photocatalytic activity of SiO₂-TiO₂ composite in a batch photoreactor using MB

The photocatalytic activity of the SiO_2-TiO₂ composite was evaluated at room temperature in the Luzchem photoreactor with lamps with a maximum emission wavelength of 352 nm and a power of 8 W each. Samples were placed at ca. 10 cm (light intensity was 3.8 mW cm⁻²). In a typical photocatalytic test, different aqueous mixtures (4 mL, each) of MB (1.5×10^{-5} M) in presence of the SiO_2-TiO₂ composite (17.5 mg mL⁻¹) were irradiated in pyrex tubes of 1.5 cm of inner diameter, at room temperature (25 °C). The photodegradation of MB was monitored at different irradiation times (up to 2 h) through UV–vis analysis. Finally, the SiO_2-TiO₂ composite was submitted to the desorption method described above to ensure the total photodegradation of the MB.

Additionally, an aqueous MB (1.5×10^{-5} M) solution was submitted to the same irradiation procedure in the absence of the photocatalyst to evaluate direct photolysis.

2.6. Photocurrent measurements

A standard three-electrode configuration was used in a homemade quartz electrochemical cell with a platinum wire as the counter electrode and a saturated Ag/AgCl reference electrode. The working electrode was prepared with the following procedure: first, a paste of each material was obtained by mixing 50 mg of photocatalyst with 0.5 mL of terpineol and 1 mL of acetone. The mixture was left stirring overnight; then, the cap was opened and left until the acetone completely evaporated. Then, 25 μL of each sample was spread onto a conductive carbon paper with dimensions of approximately 2.0×1.0 cm². The resulting final area was 1.0×1.0 cm². Finally, the electrode was sintered at 450 °C for 30 min.

The photocurrent generated by the working electrodes was measured at 0.4 V for 10 cycles of light on/off, with each cycle having a duration of 20 s. A 0.5 M Na_2SO_4 electrolyte solution was used. Prior to the measurements, the solutions were purged with argon for 10 min. UV–vis irradiation of the working electrodes was carried out with a spotlight Hamamatzu Xe lamp (Lightnincure LC8 model, 800–200 nm, 1000 W/ m², fiber optic light guide with a spot size of 0.5 cm).

2.7. Phenol mineralization by SiO₂-TiO₂ in a continuous flow SPS photoreactor

The mineralization of a solution of phenol (10^{-5} M) in Milli-Q water was evaluated at room temperature (25 °C) in a portable 35 cm³ continuous flow photoreactor filled with 7.5 g of SiO_2-TiO₂ composite. Progress of the mineralization was monitored in situ with a Total Organic Carbon (TOC, Mettler Toledo Portable TOC 450) coupled to the tubular glass photoreactor. For this purpose, Milli-Q water was circulated through the hand-made photoreactor at 10 mL min⁻¹, and a baseline was measured for 45 min to ensure a stationary flux in the

Table 1

Continuous flow photoreactor working regimes, volumetric flows (Q_{A1} and Q_{A2}), and corresponding times of residence (t_R).

Regime	Q_{A1} (mL min⁻¹)	t_R (min)	Q_{A2} (mL min⁻¹)
1	10.1	3.47	23.4
2	11.7	2.99	18.3
3	14.5	2.41	18.3
4	20.8	1.68	18.3

absence of light (Regime conditions were summarized in Table 1). Then, the value of TOC of the phenol solution (720 ppb C) was monitored for 45 min in the same conditions to ensure the TOC stabilization prior to switching on the LED irradiation system. Two homemade LED PCB structures with 40 single-color UV LEDs of 800 mW each with an irradiation band centered at $\lambda_{em} = 365$ nm were used. The tubular glass photoreactor was placed between the two LED PCB at *ca.* 1.5 cm distance to each one (the light intensity of each LED PCB at this distance of the tubular glass photoreactor was 160 mW cm^{-2}). As a control experiment, the photolysis of the phenol 10^{-5} M solution was conducted under the same conditions but with the photoreactor filled with 7.5 g of pristine glass wool.

2.8. Evaluation of the reusability of SiO$_2$-TiO$_2$ composite

The reusability test was conducted at the same conditions as employed in the flow photoreactor, *vide supra*. Hence, 7.5 g of the SiO$_2$-TiO$_2$ composite placed in the tubular glass of the hand-made photoreactor was washed with Milli Q water until the TOC signal was identical to that of the milli Q water. Then, a new P solution (1 × 10^{-5} M, 720 ppb C) was injected and recirculated for 45 min in darkness to ensure a stable value for the TOC prior to switching on the LED irradiation system. See Table 1 for the Regime conditions used in the reusability test.

3. Results and discussion

3.1. Synthesis and characterization of the SiO$_2$-TiO$_2$ composite

The SiO$_2$-TiO$_2$ composite was synthesized according to Scheme 1. First, SiO$_2$ particles of theoretical 575 nm diameter were synthesized following a previously published protocol (Scheme 1A) [46]. The following step is the formation of the shell of TiO$_2$ from titanium (IV) isopropoxide (TTIP). This step involves the hydrolysis and condensation of the precursor as the two critical reactions, as it was previously discussed by Cabezuelo *et al.* [21] . In this sense, the TTIP can be hydrolyzed by either water from the medium or the Si—OH moieties present on the surface of SiO$_2$ spheres. However, since the precursor and the SiO$_2$ spheres were mixed before the humidified airflow started, we assumed that the hydrolysis would be initiated by the Si—OH groups. As a result, one or more isopropoxide groups undergo hydrolysis, and the Ti—O—Si linkage is formed (see reaction 1).

$$Ti(O^iPr)_4 + Si\text{—}OH \rightarrow Si\text{—}O\text{—}Ti(O^iPr)_3 + {}^iPrOH \qquad (1)$$

After that, the humidified airflow starts increasing the H$_2$O molecules concentration in the EtOH matrix. Thus, Si—O—Ti(O^{i}Pr)$_3$ groups are prone to further react with H$_2$O, in a second hydrolysis reaction step (see reaction 2).

$$Si\text{—}O\text{—}Ti(O^iPr)_3 + H_2O \rightarrow Si\text{—}O\text{—}Ti(OH)(O^iPr)_2 + {}^iPrOH \qquad (2)$$
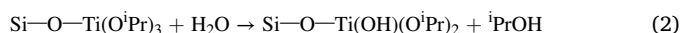
Afterward, Ti—OH groups formed are prone to condensation. This
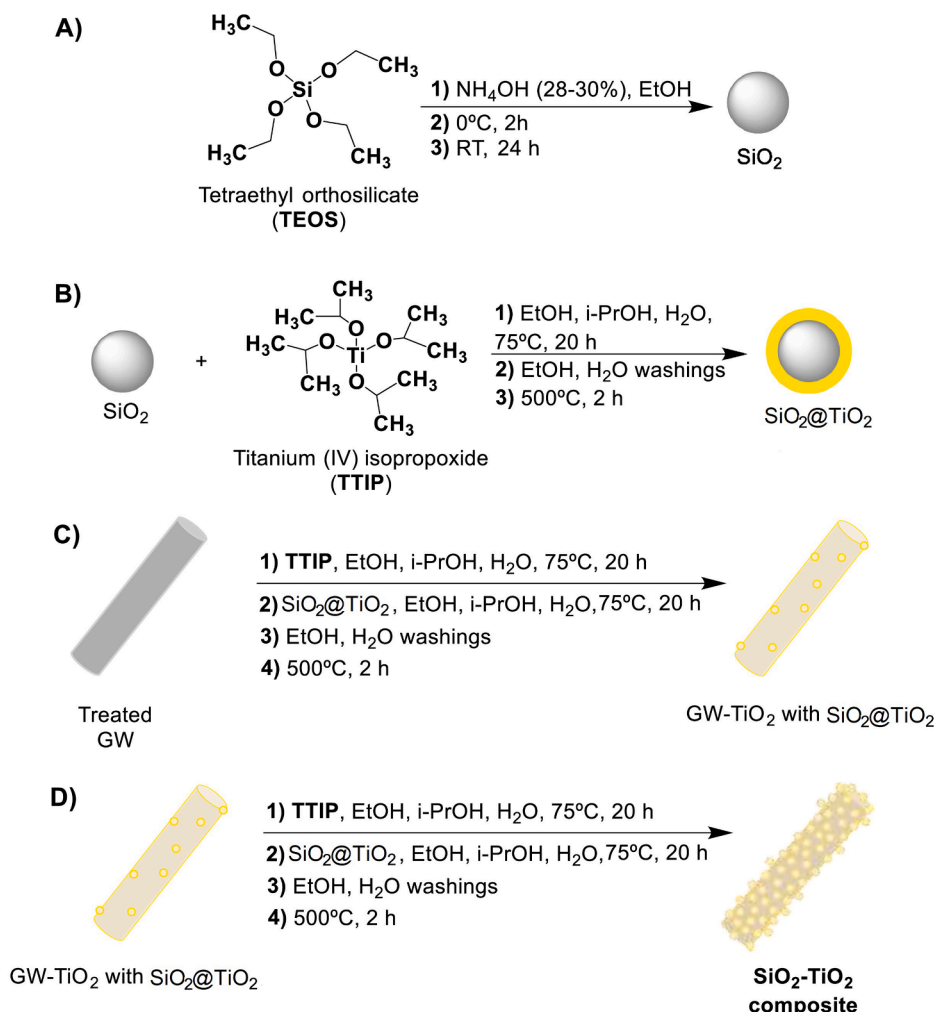
Scheme 1. Synthesis of the SiO$_2$-TiO$_2$ composite.

means that the Ti—OH groups react with other $Ti(OH)(O^iPr)_3$ present in the media to form Ti—O—Ti bonds. Finally, the H_2O molecules conduct a last hydrolysis reaction which results in the formation of a three-dimensional network of titanium and oxygen atoms.

Subsequent calcination at 500 °C for 2 h resulted in a homogeneous formation of the TiO_2 shell, see Scheme 1B. It is worth mentioning that previous studies concluded that thickness values between *ca.* 10 nm and *ca.* 50 nm provide the best photo-reactivity of $SiO_2@TiO_2$ materials [16–21]. Thus, the amount of TTIP in this step was first estimated on the basis of the diameter of the SiO_2 particles to afford $SiO_2@TiO_2$ spheres with a complete shell of TiO_2 with a 20 nm thickness (see Supporting Information Section I). Nevertheless, assuming that the expected shell will leave empty spaces among the crystals, this amount was considered excessive. In fact, the best results were obtained when only 2/3 of the theoretical amount was used. In parallel, the commercial GW was washed under acidic media, followed by a basic wash in an NH_4OH solution. Then, it was successively washed with water until pH 10 and dried at 100 °C for 24 h. The washed GW was submitted to a TiO_2 coating procedure. A few geometrical assumptions were made to estimate the theoretical amount of TTIP needed to get *ca.* 20 nm thickness for the coating (see details in SI); eventually, the best results were obtained with this theoretical amount. Next, it was submitted to a decoration procedure with the $SiO_2@TiO_2$ spheres for 20 h, followed by

calcination, see Scheme 1C. Again, we estimated the ratio $SiO_2@TiO_2$ spheres/GW in an attempt to get complete coverage of the surface. The best results were found when a slight defect of this ratio was employed. Nevertheless, the protocol was improved with a second decoration step that resulted in an enhanced number of $SiO_2@TiO_2$ spheres on the surface (Scheme 1D). Finally, the SiO_2-TiO_2 composite was calcinated to achieve the anatase photoactive phase for TiO_2.

TEM analysis demonstrates a spherical shape for SiO_2 particles, which is preserved after the TiO_2 coating, as can be seen in the representative TEM images in Fig. 1.
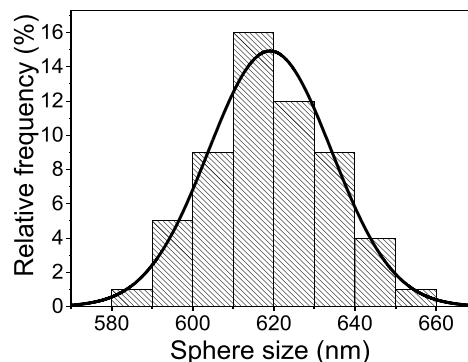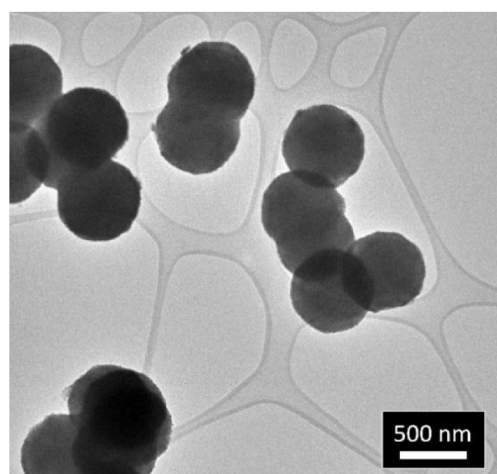
Furthermore, the corresponding size distributions for SiO_2 spheres display an average diameter of 575 ± 16 nm for the SiO_2 spheres, which is enlarged up to 619 ± 15 nm after the TiO_2 coating process. The morphology and the TiO_2 shell structure of the synthesized $SiO_2@TiO_2$ spheres, together with the SiO_2-TiO_2 composite, were investigated through FESEM. SiO_2 spheres display a smooth surface (Fig. 2(A)), while the surface of the $SiO_2@TiO_2$ spheres is rougher as a result of a homogenous TiO_2 nanocrystal shell (Fig. 2(B)). Moreover, pristine GW is composed of cylindrical fibers with a soft surface (Fig. 2(C)), which, as expected, increases its texture and roughness after the TiO_2 coating process (Fig. 2(D)).

For a deeper analysis of the SiO_2-TiO_2 composite surface, trenches were performed to evaluate the TiO_2 layer thickness after the TiO_2
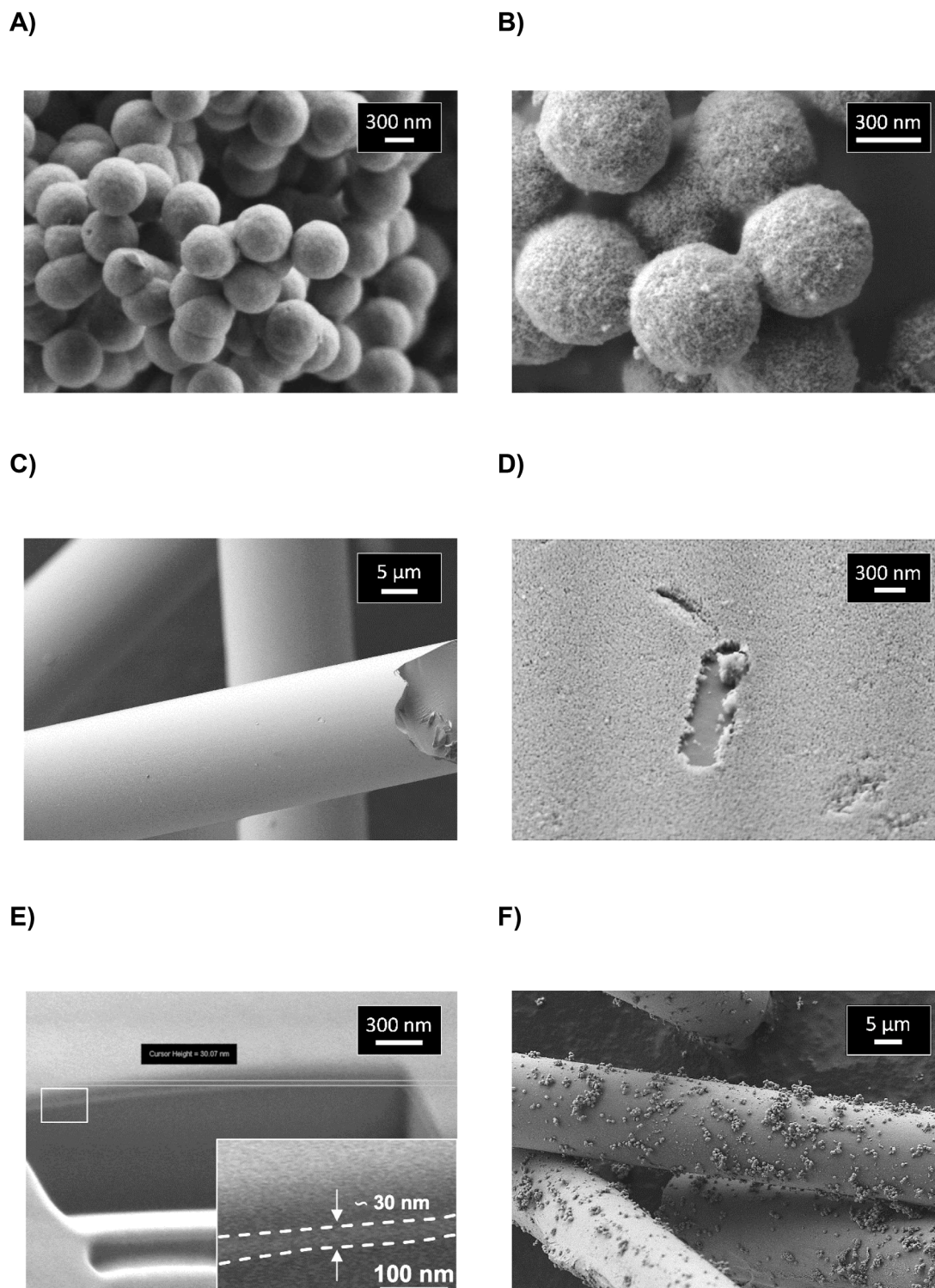
A)
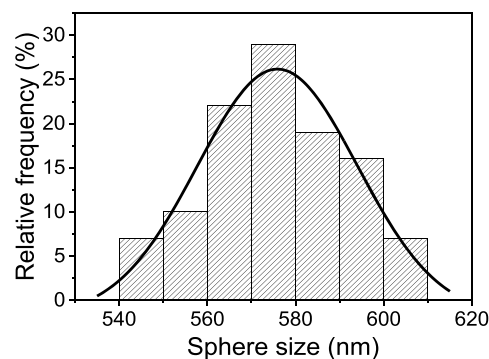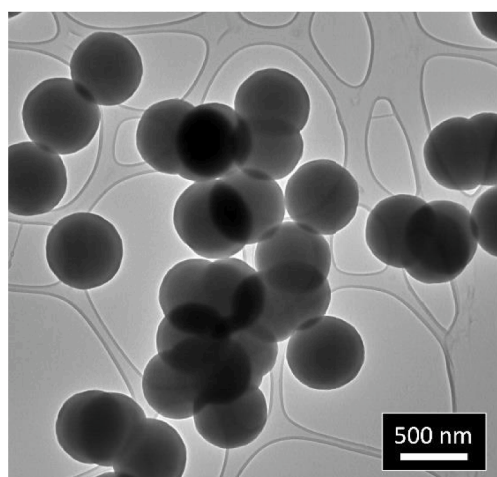
B)

Fig. 1. TEM images and corresponding size distribution for SiO_2 (A) and $SiO_2@TiO_2$ (B) spheres.

A)

B)

C)

D)

E)

F)

Fig. 2. FESEM images of SiO$_2$ spheres (A), SiO$_2$@TiO$_2$ spheres (B), pristine glass wool (C), TiO$_2$ layer of the SiO$_2$-TiO$_2$ composite (D), trench performed on the TiO$_2$ layer of the SiO$_2$-TiO$_2$ composite surface with FIB (E), and SiO$_2$-TiO$_2$ composite (F).

coating process. In this sense, Fig. 2(E) shows the obtained TiO$_2$ shell (thickness of *ca.* 30 nm) over the GW on the SiO$_2$-TiO$_2$ composite. As expected from the careful design of the synthetic protocol, the obtained TiO$_2$ thickness layer corresponds to values between those described as the optimum TiO$_2$ thickness for photocatalytic processes of SiO$_2$@TiO$_2$ materials [16–20]. Finally, the number of SiO$_2$@TiO$_2$ spheres decorating the SiO$_2$-TiO$_2$ composite is high, and they are homogeneously distributed throughout the SiO$_2$-TiO$_2$ composite surface, as can be seen in Fig. 2(F).

N$_2$ adsorption-desorption isotherms (see Fig. S4 of SI section 2) on the SiO$_2$@TiO$_2$ spheres showed typical type II curves and H3 hysteresis usually found for solids consisting of aggregates of particles with irregular cylindrical pores [47,48]. Besides, the estimated BET surface area was 27.3 ± 0.1 m^2 g^{-1}. In the case of the SiO$_2$-TiO$_2$ composite, it displayed a BET surface area of 0.9 m^2 g^{-1}, which, although it is lower than that of the spheres, represented a significant enhancement

compared to that of the pristine GW. In fact, a value of 0.09 m^2 g^{-1} was calculated for the surface of GW, assuming that GW is a single cylindrical fiber (more details in SI, Section 1). In this manner, N$_2$ adsorption-desorption measurements were also performed for uncoated treated GW but, as shown in SI Section 2, inconclusive results were obtained. Hence, this surface increase can mainly be attributed to the high number of SiO$_2$@TiO$_2$ spheres decorating the SiO$_2$-TiO$_2$ composite.

X-ray diffraction (XRD) patterns and Raman spectroscopy confirmed the anatase crystalline phase of the TiO$_2$ on the shell of the SiO$_2$@TiO$_2$ spheres. Fig. 3(A) shows a broad peak centered at a 2-theta value of 22°, which is characteristic of amorphous silica. Nevertheless, the representative TiO$_2$ anatase peaks at 2-theta values of 25°, 38°, 48°, 55°, and 63° act as proof of the selective crystallization into the photoactive TiO$_2$ crystal phase upon calcination at 500 °C [49]. The crystal size of the TiO$_2$ nanocrystals from the SiO$_2$@TiO$_2$ spheres shell was *ca.* 11.8 nm from the Scherrer equation to the 2-theta 25° peak, which corresponds
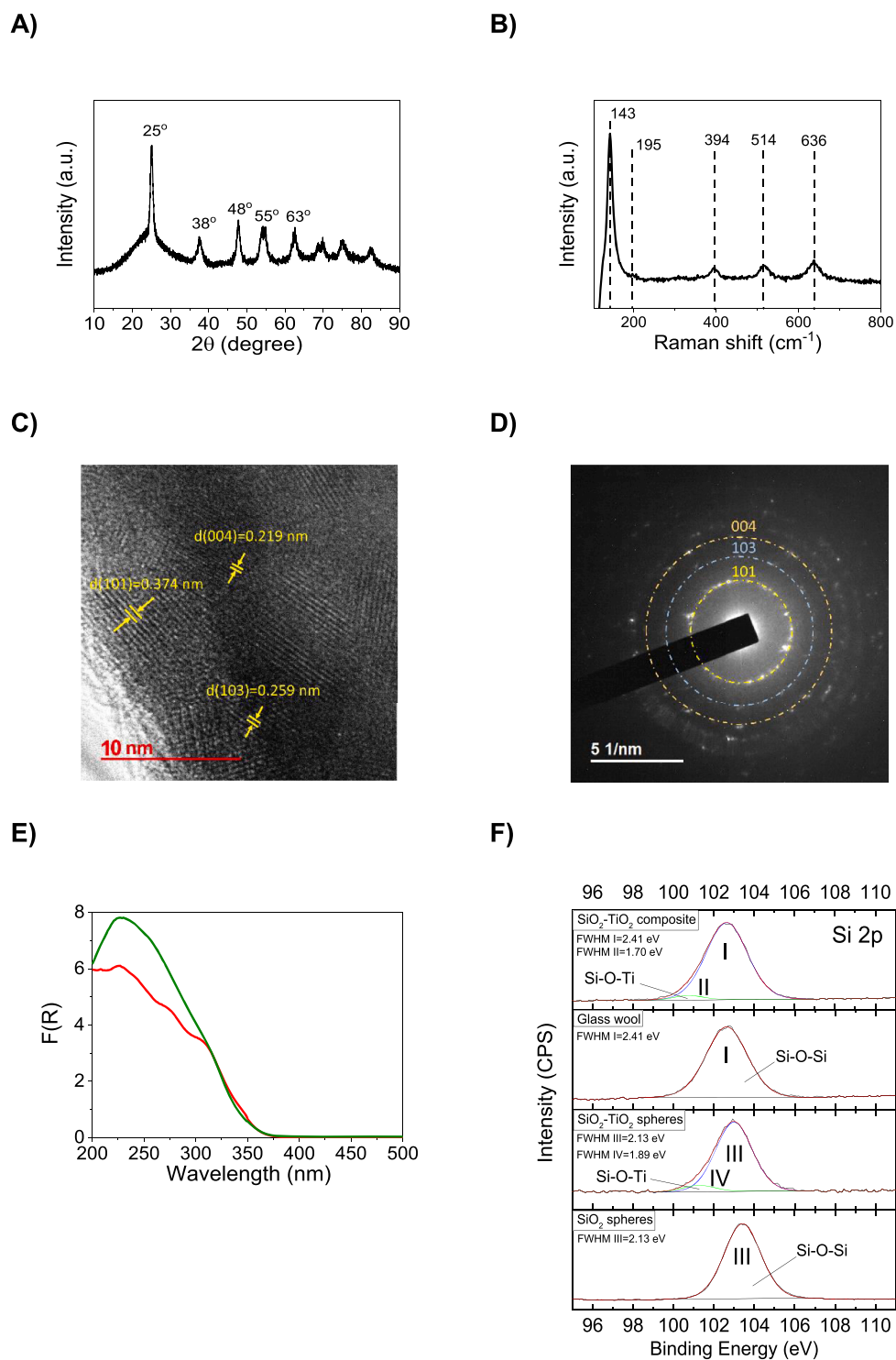
Fig. 3. X-ray diffractogram (A) and Raman spectrum (B) of the SiO$_2$@TiO$_2$ spheres; HRTEM image (scale of 10 nm) (C) and SAED pattern of the SiO$_2$-TiO$_2$ composite; Diffuse reflectance spectra of the SiO$_2$@TiO$_2$ spheres (red line) and SiO$_2$-TiO$_2$ composite (green line) (E); X-ray Photoelectron Spectroscopy (XPS) spectra of Si 2p core level (F).

to the (101) lattice plane of anatase (see more details in SI section 2 and Fig. S5) [50]. The TiO_2 anatase phase on the SiO_2@TiO_2 spheres was also confirmed by Raman spectroscopy (Fig. 3(B)): E_g (143 cm^{-1}), E_g (195 cm^{-1}), B_{1g} (394 cm^{-1}), A_{1g} (514 cm^{-1}), E_g (636 cm^{-1}) [51]. In the case of the SiO_2-TiO_2 composite, the TiO_2/SiO_2 mass ratio is below the sensitivity of the equipment to be able to disclose the TiO_2 anatase signals (see Fig. S6). Nevertheless, as the SiO_2-TiO_2 composite has undergone the same calcination procedure as the SiO_2@TiO_2 spheres, it can be assumed that the TiO_2 on the surface of the composite has crystallized into the anatase photoactive phase. Accordingly, HRTEM analysis of the SiO_2-TiO_2 composite confirmed the crystalline nature of the TiO_2 in the final photocatalyst. Thus, interplanar distances of 0.374 nm, 0.259 nm, and 0.219 nm were found in the TiO_2 nanocrystals, which correspond to (101), (103), and (004) lattice planes of anatase (Fig. 3 (C)) [52]. These results are consistent with the outcomings provided by the selected area electron diffraction (SAED) pattern (Fig. 3(D)). The study also revealed that the SiO_2@TiO_2 spheres were attached to the GW surface through a thin TiO_2 film (see Section S2 of SI, Fig. S7B).

The optical properties of the SiO_2-TiO_2 composite were investigated by diffuse reflectance spectroscopy, and the results were represented as the Kubelka–Munk function *vs.* wavelength [53]. As it is shown in Fig. 3 (E), the optical behavior of the SiO_2-TiO_2 composite does not differ from the one displayed by the SiO_2@TiO_2 spheres, both showing a wide absorption band from 200 nm to 375 nm. However, in comparison to unsupported commercial TiO_2, the spheres and the composite show a blue shift which might be caused by the slight difference in the TiO_2 crystal size and the different light scattering ability of the samples, as it has been previously described for similar materials [20].

An extensive X-ray Photoelectron Spectroscopy (XPS) analysis was performed in order to investigate the nature of the chemical bonding between the elements in the SiO_2-TiO_2 composite and in the SiO_2@TiO_2 spheres (Fig. 3(F) and in SI section 2 Fig. S8).

The Si 2p core level spectra of both SiO_2-TiO_2 composite and the pristine GW (Fig. 3(F)) present a main component at 102.7 eV, which fitted a Full Width at Half Maximum (FWHM) I of 2.41 eV, that was ascribed to the Si—O—Si bond. This band occurs at slightly lower binding energy (BE) than the one observed in the case of the SiO_2@TiO_2 and SiO_2 spheres, which present a main component at 103.03 eV and 103.41 eV, respectively (FWHM III of 2.13 eV), that was safely assigned to the Si—O—Si linkage [16]. Furthermore, the spectrum for the SiO_2-TiO_2 composite shows an additional component (FWHM II = 1.70 eV) at 2.0 eV lower BE, which can be attributed to the Si—O—Ti bond. Analogously, the XPS for the SiO_2@TiO_2 spheres shows an additional component (FWHM IV = 1.89 eV) at 1.73 eV lower BE that indicates the formation of an interfacial Si—O—Ti linkage, as reported previously for SiO_2@TiO_2 core@shell nanoparticles [20,54]. Additional results obtained from the analysis of the O 1s and Ti 2p core levels (see Fig. S8) agree with those for Si 2p level. Overall, the XPS of the SiO_2-TiO_2 composite provides evidence of the linkage Si—O—Ti and the anatase form of the crystalline TiO_2 in the SiO_2@TiO_2 spheres and in the SiO_2-TiO_2 composite.

Finally, from the IOP-OES analysis, the TiO_2 loading on the SiO_2@-TiO_2 spheres was 19.7 % TiO_2 (w/w), and a value of 1.1 % (w/w) was found for the SiO_2-TiO_2 composite.

After overall characterization, it was confirmed that both the SiO_2 cores and GW were homogeneously covered by a TiO_2 nanocrystal shell with a thickness value ranging between 22 and 30 nm. Indeed, this range is set as an optimal TiO_2 thickness shell to produce high photocatalytic efficiency in SiO_2@TiO_2 materials [16–20].

3.2. Adsorption-desorption capacity of the SiO_2-TiO_2 composite

Adsorption-desorption capacity of Methylene Blue (MB) over the SiO_2-TiO_2 composite surface was analyzed before studying the MB degradation using this photocatalyst in a batch photoreactor. Hence, using UV–vis spectroscopy it was observed that the SiO_2-TiO_2 composite

is able to adsorb *ca.* 30 % of this dye at 1.5×10^{-5} M (see Fig. S12). This process likely followed a monolayer adsorption model based on the Langmuir isotherm [55]. In this sense, TiO_2 materials at the experimental pH (*ca.* pH 7) display negative values for its ζ-potential [56] while MB is cationic. Thus, the transference of MB from the aqueous phase to the solid phase continues until the equilibrium is reached [57], giving rise to a MB monolayer on the TiO_2 surface and a remnant amount of MB molecules in the solution. Afterward, a desorption test was performed to ensure an efficient MB recovery from the SiO_2-TiO_2 composite surface and to guarantee a correct mass balance (see Fig. S12). Interestingly, when the adsorption study was performed using phenol (1×10^{-5} M) as the selected recalcitrant pollutant, no adsorption was observed on the SiO_2-TiO_2 composite. Thereby, both registered UPLC chromatograms and UV–vis spectra from the aliquots taken at different times under dark conditions did not show any change.

3.3. Evaluation of the photocatalytic activity of the SiO_2-TiO_2 composite

Initially, the photocurrent response of the composite was evaluated to provide evidence of its charge separation (see Fig. S10). Thus, the chronoamperometry curve of the prepared photocatalyst electrode from the SiO_2@TiO_2 spheres showed activity, confirming an enhanced charge separation efficiency [58,59]. However, for the SiO_2-TiO_2 composite, the TiO_2 weight was below the sensitivity of the equipment to be able to record any photocurrent response.

Nevertheless, the photocatalytic activity of the SiO_2-TiO_2 composite was further evaluated against MB as a model organic compound using a batch photoreactor. For this purpose, aqueous solutions of MB (1.5×10^{-5} M) were irradiated with light centered at $\lambda_{em} = 352$ nm in the presence of the SiO_2-TiO_2 composite (17.5 mg mL^{-1}). Photolysis of MB was also studied in the absence of the photocatalyst as a control experiment. The experiments were monitored by UV–vis spectroscopy following the absorption peak at 664 nm for MB (Fig. 4). The photocatalytic degradation mediated by the SiO_2-TiO_2 composite achieved the elimination of 80 % of MB in the first 30 min, fulfilling its total elimination in 120 min (Fig. 4). In this context, direct photolysis of MB only accounted for 20 % of the observed degradation upon 120 min irradiation. These results unambiguously demonstrated the photocatalytic activity of the new composite regardless of the mechanism of the photocatalyzed MB degradation.
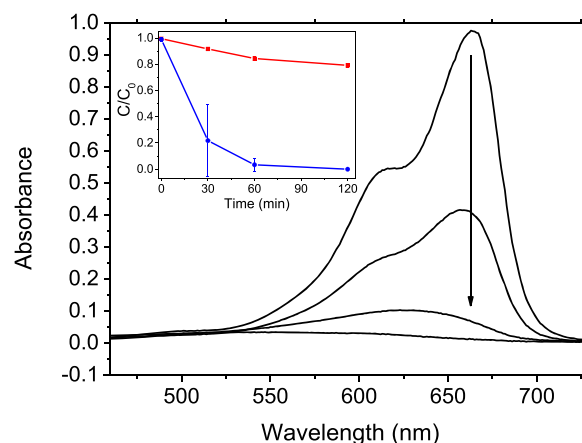

Fig. 4. Representative UV–vis spectra of the photocatalytic degradation of an aerated aqueous solution of MB (1.5×10^{-5} M) in the presence of SiO_2-TiO_2 composite (17.5 mg mL^{-1}) at 0, 30, 60, and 120 min of irradiation with UVA light centered at $\lambda_{em} = 352$ nm. Inset: comparative MB photodegradation in the presence (●) and absence (■) of the SiO_2-TiO_2 photocatalyst.

3.4. Phenol mineralization using SiO2-TiO2 composite in a continuous flow photoreactor

Once we had tested the photocatalytic activity of the SiO2-TiO2 composite using MB as a representative organic pollutant model, we investigated its potential in a flow photoreactor against phenol, a real recalcitrant contaminant. Hence, a continuous flow SPS photoreactor at a laboratory scale was designed to evaluate the photocatalytic efficiency of SiO2-TiO2 using aqueous solutions of phenol. Scheme 2 shows the diagram of the designed continuous flow photoreactor at a lab scale, which is composed of a 35 cm^3 tubular glass column (R) surrounded by two independent UV-A LED (λ_{em} = 365 nm) PCBs modules (L1 and L2) (see more details in Fig. S13), two peristaltic pumps (P1 and P2), two feeding tanks: feeding tank 1 containing the contaminated water (F1), and feeding tank 2 (F2) which contains Mili-Q water; and a distributor (D) which injects the sample at a fixed flow (Q_T) of 20 mL min^{-1} in a continuous Total Organic Carbon analyzer (T). This design provides a high photocatalytic area due to the efficient illumination system and an improved pollutant mass transport from the water phase to the photocatalyst surface as a result of the fine contact within the photoreactor.

The volumetric flow (Q_{A1}) that enters the photoreactor column (R) sets the time of residence (t_R) of the solution. However, the current that exits the column encounters another stream modulated by another volumetric flow of Mili-Q water (Q_{A2}). This dilutes the sample prior to its injection into the continuous Mettler Toledo Portable TOC 450 analyzer (Q_T). Finally, the excess volume from the distributor (D), together with the one that has already been analyzed by the TOC, is disposed of in the waste tank (W).

A phenol solution (1 × 10^{-5} M, 720 ppb C) prepared in Milli-Q water was injected through the column of the photoreactor, which was filled with 7.5 g of the SiO2-TiO2 composite. Four different regimes were evaluated to find the most efficient residence time (Table 1), and the results are shown in Fig. 5 (see also control experiments replacing the composite with pristine GW, SI, section 4, Fig. S14).

Fig. 5(A) shows the results obtained from Regime 1 and Regime 2 sequentially. Both regimes showed similar results. Thus, a drastic drop in TOC signal was produced ca. 15 min after initiating the irradiation until total mineralization of the phenol solution was achieved, remaining stable and below the Milli-Q water baseline during the rest of the irradiation time. In Regime 1, mineralization was achieved upon flowing across the illuminated zone filled with photocatalyst in just 3.47 min, while in Regime 2, only 2.99 min were needed. Under Regime 2, the arriving flow to the TOC detector was less diluted, increasing the initial

TOC signal accordingly. Furthermore, the conductivity of the phenol solutions was also measured in situ (see Fig. 5(A) blue line). A small increase in the water conductivity was observed as the TOC concentration decreased, which might be explained by the acid-base equilibrium of generated CO2. Fig. 5(B) and (C) show the results obtained for the P mineralization under regimes 3 and 4, respectively, without changing the photocatalyst. As expected, from the lower residence times (2.41 min and 1.68 min, respectively), the final level of mineralization achieved was lower (18 % and 40 % of initial values, respectively). However, in both cases, although a fast decay of the TOC signal to almost total mineralization was observed in the first irradiation minutes, the value of the TOC increased again, reaching a plateau. This increment can be given by photoproducts, which will remain adsorbed over the SiO2-TiO2 composite surface. During the irradiation time, these by-products might be released into the aqueous solution due to the low residence times in the photoreactor. Thus, there may not be enough time to remove these molecules, so they are moved away by the water flow, increasing the TOC signal in time. Consecutive off/on cycles gave identical results. In this context, it is important to mention that phenol oxidation to total mineralization must occur following the mechanism already described in the literature for TiO2 because SiO2 supports are inert and do not change the mechanism of action of the TiO2 photocatalyst [60]. Even more important was the fact that the composite remained unchanged over the experiment (a total of 17.5 liters of phenol solution), keeping its efficiency. Accordingly, no leaching of titanium was found by ICP-OES analysis of the treated aqueous samples. In addition, XPS and FESEM analysis of the SiO2-TiO2 composite before and after a further photocatalytic reaction with phenol were performed to evaluate the stability of the photocatalyst (see Figs. S9 and S11, respectively). Both studies revealed the great robustness of the photocatalyst, as the material remained unaltered during its photocatalytic application. For instance, XPS spectra showed no variation in the Si—O—Ti component of the Si2p core level, confirming the absence of TiO2 leaching from the photocatalyst, which was in agreement with the assay carried out by ICP-OES. Accordingly, FESEM images disclosed no sign of deterioration of the SiO2-TiO2 composite after the photocatalytic reaction.

Thereby, all results have demonstrated that the SiO2-TiO2 composite kept its photocatalytic activity during the mineralization of ca. 20 liters of polluted solution (P at 1 × 10^{-5} M) due to the robust nature of the photocatalyst under the irradiation conditions in a continuous flow photoreactor. Adjusting operational parameters, such as the flow of contaminated water, the intensity of light, and the loading of the
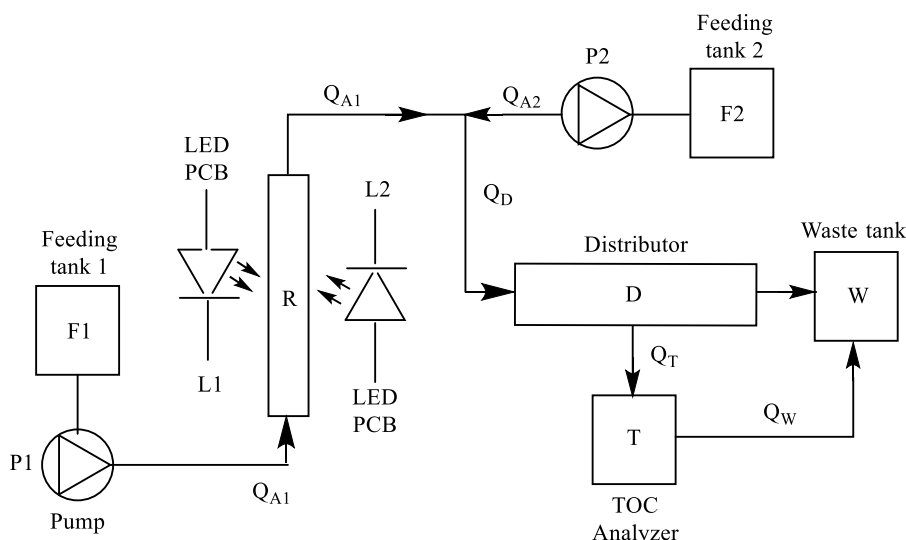
Scheme 2. Diagram of the homemade continuous flow photoreactor at a lab scale.

A)

B)

C)
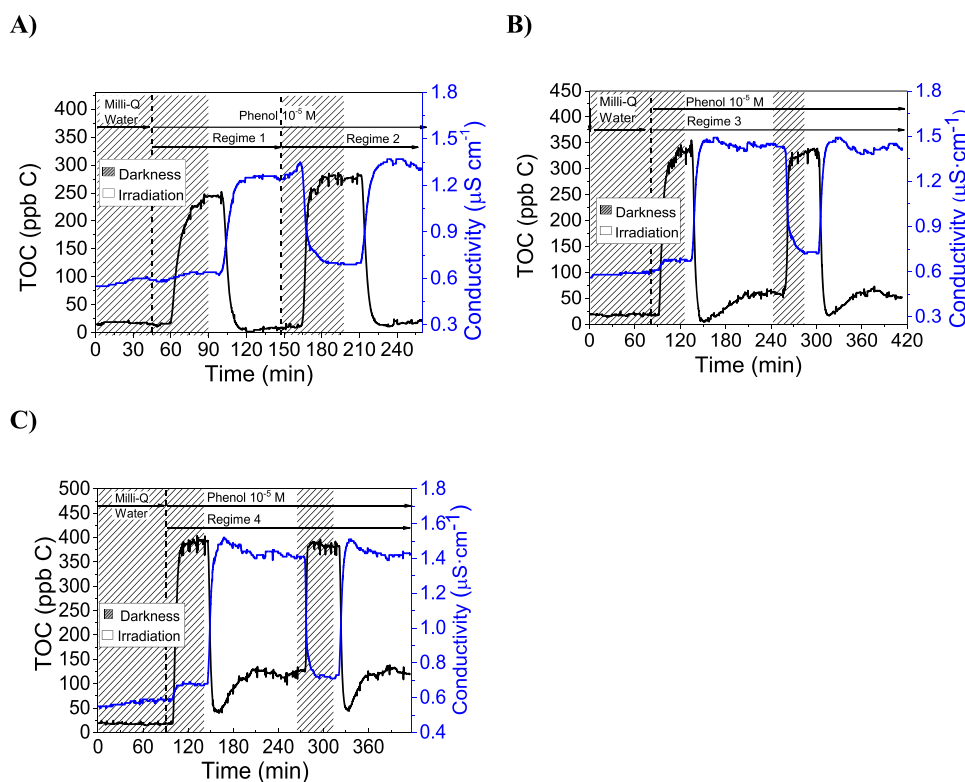
Fig. 5. Photocatalytic mineralization of Phenol (1×10^{-5} M) aqueous solution, conducted in the continuous flow photoreactor filled with 7.5 g of SiO_2-TiO_2 composite under UV-A irradiation (λ_{max}=365 nm) at working Regime 1 and Regime 2 (A); Regime 3 (B) and Regime 4 (C).

photocatalyst, allowed the achievement of total mineralization of organic recalcitrant pollutants in a short time [61]. Therefore, by merging a large surface area and the optimal TiO_2 thickness on both GW (used as a macroscopic support) and SiO_2@TiO_2 microspheres (to increase the surface area), we have developed an effective photocatalyst for continuous flow SPS photoreactors.

4. Conclusions

A robust SiO_2-TiO_2 composite is presented as a novel and highly efficient photocatalyst that surpasses the disadvantages of traditional wastewater treatment methods and overcomes the deficiencies of established titania-supported materials. For instance, the new SiO_2-TiO_2 composite offers an optimized TiO_2 layer thickness (20–30 nm), and its photocatalytic area was increased by an innovative strategy. Hence, the new photocatalyst was synthesized by attaching micrometric SiO_2@-TiO_2 core-shell spheres to a TiO_2-covered glass wool (GW) support. The highly efficient photoactivity of the SiO_2-TiO_2 composite was demonstrated by investigating the mineralization of a phenol solution (ppm range). Even though phenol does not adsorb on the photocatalyst, it was mineralized in less than three minutes at a continuous flow regime.

Even more, results revealed that this photocatalyst can be easily implemented as a fixed-bed in continuous flow (SPS) photoreactors at plant scale for wastewater remediation because its reuse does not require filtration procedures and it does not leach titania.

Declaration of Competing Interest

The authors declare that they have no known competing financial interests or personal relationships that could have appeared to influence the work reported in this paper.

Data availability

No data was used for the research described in the article.

Acknowledgments

Supplementary materials

Supplementary material associated with this article can be found, in the online version, at doi:10.1016/j.apmt.2023.101947.

References

[1] U. von Gunten, Oxidation processes in water treatment: are we on track? Environ. Sci. Technol. 52 (2018) 5062–5075, https://doi.org/10.1021/acs.est.8b00586.

[2] D. Ma, H. Yi, C. Lai, X. Liu, X. Huo, Z. An, L. Li, Y. Fu, B. Li, M. Zhang, L. Qin, S. Liu, L. Yang, Critical review of advanced oxidation processes in organic wastewater treatment, Chemosphere 275 (2021) 130104, https://doi.org/10.1016/j.chemosphere.2021.130104.

[3] J.-M. Herrmann, Heterogeneous photocatalysis: fundamentals and applications to the removal of various types of aqueous pollutants, Catal. Today 53 (1999) 115–129, https://doi.org/10.1115/IMECE200743738.

[4] H. Gerischer, The impact of semiconductors on the concepts of electrochemistry, Electrochim. Acta 35 (1990) 1677–1699, https://doi.org/10.1016/0013-4686(90)87067-C.

[5] S. Malato, J. Blanco, A. Vidal, C. Richter, Photocatalysis with solar energy at a pilot-plant scale: an overview, Appl Catal B 37 (2002) 1–15, https://doi.org/10.1016/S0926-3373(01)00315-0.

[6] D. Zhou, H. Luo, F. Zhang, J. Wu, J. Yang, H. Wang, Efficient photocatalytic degradation of the persistent PET fiber-based microplastics over Pt nanoparticles decorated N-doped TiO_2 nanoflowers, Adv. Fiber Mater. 4 (2022) 1094–1107, https://doi.org/10.1007/s42765-022-00149-4.

[7] X. Li, T. Liu, Y. Zhang, J. Cai, M. He, M. Li, Z. Chen, L. Zhang, Growth of BiOBr/ZIF-67 nanocomposites on carbon fiber cloth as filter-membrane-shaped photocatalyst for degrading pollutants in flowing wastewater, Adv. Fiber Mater. 4 (2022) 1620–1631, https://doi.org/10.1007/s42765-022-00189-w.

[8] A. Zapata, T. Velegraki, J.A. Sánchez-Pérez, D. Mantzavinos, M.I. Maldonado, S. Malato, Solar photo-Fenton treatment of pesticides in water: effect of iron concentration on degradation and assessment of ecotoxicity and biodegradability, Appl. Catal. B 88 (2009) 448–454, https://doi.org/10.1016/j.apcatb.2008.10.024.

[9] B. Weng, M.-Y. Qi, C. Han, Z.-R. Tang, Y.-J. Xu, Photocorrosion inhibition of semiconductor-based photocatalysts: basic principle, current development, and future perspective, ACS Catal. 9 (2019) 4642–4687, https://doi.org/10.1021/acscatal.9b00313.

[10] S. Malato, J. Blanco, A. Campos, J. Cáceres, C. Guillard, J.M. Herrmann, A. R. Fernández-Alba, Effect of operating parameters on the testing of new industrial titania catalysts at solar pilot plant scale, Appl. Catal. B 42 (2003) 349–357, https://doi.org/10.1016/S0926-3373(02)00270-9.

[11] Y. Abdel-Maksoud, E. Imam, A. Ramadan, TiO2 solar photocatalytic reactor systems: selection of reactor design for scale-up and commercialization—Analytical review, Catalysts 6 (2016) 138, doi:10.3390/catal6090138.

[12] Z. Zahra, Z. Habib, S. Chung, M.A. Badshah, Exposure route of TiO2 NPs from industrial applications to wastewater treatment and their impacts on the agro-environment, Nanomaterials 10 (2020), https://doi.org/10.3390/nano10081469.

[13] P.S. Mukherjee, A.K. Ray, Major challenges in the design of a large-scale photocatalytic reactor for water treatment, Chem. Eng. Technol. 22 (1999) 253–260, https://doi.org/10.1002/(SICI)1521-4125(199903)22:3<253::AID-CEAT253>3.0.CO;2-X.

[14] B. Erjavec, P. Hudoklin, K. Perc, T. Tišler, M.S. Dolenc, A. Pintar, Glass fiber-supported TiO_2 photocatalyst: efficient mineralization and removal of toxicity/estrogenicity of bisphenol A and its analogs, Appl. Catal. B 183 (2016) 149–158, https://doi.org/10.1016/j.apcatb.2015.10.033.

[15] A.K. Ray, A. Beenackers, A photocatalytic reactor for water purification and use thereof, WO1997037936A1, 1997.

[16] S. Ullah, E.P. Ferreira-Neto, A.A. Pasa, C.C.J. Alcântara, J.J.S. Acuña, S.A. Bilmes, M.L. Martínez Ricci, R. Landers, T.Z. Fermino, U.P. Rodrigues-Filho, Enhanced photocatalytic properties of core@shell SiO_2@TiO_2 nanoparticles, Appl. Catal. B 179 (2015) 333–343, https://doi.org/10.1016/j.apcatb.2015.05.036.

[17] P.A. Williams, C.P. Ireland, P.J. King, P.A. Chater, P. Boldrin, R.G. Palgrave, J. B. Claridge, J.R. Darwent, P.R. Chalker, M.J. Rosseinsky, Atomic layer deposition of anatase TiO_2 coating on silica particles: growth, characterization and evaluation as photocatalysts for methyl orange degradation and hydrogen production, J. Mater. Chem. 22 (2012) 20203–20209, https://doi.org/10.1039/c2jm33446a.

[18] M. Ye, Q. Zhang, Y. Hu, J. Ge, Z. Lu, L. He, Z. Chen, Y. Yin, Magnetically recoverable core-shell nanocomposites with enhanced photocatalytic activity, Chemistry 16 (2010) 6243–6250, https://doi.org/10.1002/chem.200903516.

[19] F. Wang, L. Feng, Y. Qin, T. Zhao, H. Luo, J. Zhu, Dual functional SiO_2@TiO_2 photonic crystals for dazzling structural colors and enhanced photocatalytic activity, J. Mater. Chem. C 7 (2019) 11972–11983, https://doi.org/10.1039/c9tc03426a.

[20] E.P. Ferreira-Neto, S. Ullah, M.B. Simões, A.P. Perissinotto, F.S. de Vicente, P.L. M. Noeske, S.J.L. Ribeiro, U.P. Rodrigues-Filho, Solvent-controlled deposition of titania on silica spheres for the preparation of SiO_2@TiO_2 core@shell nanoparticles with enhanced photocatalytic activity, Colloids Surf. A 570 (2019) 293–305, https://doi.org/10.1016/j.colsurfa.2019.03.036.

[21] O. Cabezuelo, A. Diego-Lopez, P. Atienzar, M.L. Marin, F. Bosca, Optimizing the use of light in supported TiO_2 photocatalysts: relevance of the shell thickness, J. Photochem. Photobiol. A 444 (2023), 114917, https://doi.org/10.1016/j.jphotochem.2023.114917.

[22] N. Mandzy, E. Grulke, T. Druffel, Breakage of TiO2 agglomerates in electrostatically stabilized aqueous dispersions, Powder Technol. 160 (2005) 121–126, https://doi.org/10.1016/j.powtec.2005.08.020.

[23] D. Tarn, C.E. Ashley, M. Xue, E.C. Carnes, J.I. Zink, C.J. Brinker, Mesoporous silica nanoparticle nanocarriers: biofunctionality and biocompatibility, Acc. Chem. Res. 46 (2013) 792–801, https://doi.org/10.1021/ar3000986.

[24] R.W. Matthews, Solar-electric water purification using photocatalytic oxidation with TiO2 as a stationary phase, Sol. Energy 38 (1987) 405–413, https://doi.org/10.1016/0038-092X(87)90021-1.

[25] S. Yaparatne, C.P. Tripp, A. Amirbahman, Photodegradation of taste and odor compounds in water in the presence of immobilized TiO_2-SiO_2 photocatalysts, J. Hazard. Mater. 346 (2018) 208–217, https://doi.org/10.1016/j.jhazmat.2017.12.029.

[26] E.P. Ferreira-Neto, S. Ullah, V.P. Martinez, J.M.S.C. Yabarrena, M.B. Simões, A. P. Perissinotto, H. Wender, F.S. de Vicente, P.L.M. Noeske, S.J.L. Ribeiro, U. P. Rodrigues-Filho, Thermally stable SiO_2@TiO_2 core@shell nanoparticles for application in photocatalytic self-cleaning ceramic tiles, Mater. Adv. 2 (2021) 2085–2096, https://doi.org/10.1039/d0ma00785d.

[27] D. Chen, A.K. Ray, Photodegradation kinetics of 4-nitrophenol in TiO2 suspension, Water Res. 32 (1998) 3223–3234, https://doi.org/10.1016/S0043-1354(98)00118-3.

[28] A.K. Ray, A.A.C.M. Beenackers, Novel Swirl-Flow Reactor for Kinetic Studies of Semiconductor Photocatalysis, AIChE J. 43 (1997) 2571–2578, https://doi.org/10.1002/aic.690431018.

[29] C.M. Leroy, M.F. Achard, O. Babot, N. Steunou, P. Massé, J. Livage, L. Binet, N. Brun, R. Backov, Designing nanotextured vanadium oxide-based macroscopic fibers: application as alcoholic sensors, Chem. Mater. 19 (2007) 3988–3999, https://doi.org/10.1021/cm0711966.

[30] N. Kinadjian, M.Le Bechec, C. Henrist, E. Prouzet, S. Lacombe, R. Backov, Varying TiO2 macroscopic fiber morphologies toward tuning their photocatalytic properties, ACS Appl. Mater. Interfaces 6 (2014) 11211–11218, https://doi.org/10.1021/am501344e.

[31] D. Li, Y. Xia, Fabrication of titania nanofibers by electrospinning, Nano Lett. 3 (2003) 555–560, https://doi.org/10.1021/nl034039o.

[32] Z. Liu, D.D. Sun, P. Guo, J.O. Leckie, An efficient bicomponent TiO_2/SnO_2 nanofiber photocatalyst fabricated by electrospinning with a side-by-side dual spinneret method, Nano Lett. 7 (2007) 1081–1085, https://doi.org/10.1021/nl061898e.

[33] T. Zhao, Z. Liu, K. Nakata, S. Nishimoto, T. Murakami, Y. Zhao, L. Jiang, A. Fujishima, Multichannel TiO_2 hollow fibers with enhanced photocatalytic activity, J. Mater. Chem. 20 (2010) 5095–5099, https://doi.org/10.1039/c0jm00484g.

[34] D.N. Jadhav, A.K. Vangara, Removal of phenol from waste water using sawdust, polymerized sawdust and carbon sawdust, Indian Journal of Chemical Technologie 11 (2004) 35–41.

[35] G.S. Veeresh, P. Kumar, I. Mehrotra, Treatment of phenol and cresols in upflow anaerobic sludge blanket (UASB) process: a review, Water Res. 39 (2005) 154–170, https://doi.org/10.1016/j.watres.2004.07.028.

[36] E.-S.Z. El-Ashtoukhy, Y.A. El-Taweel, O. Abdelwahab, E.M. Nassef, Treatment of petrochemical wastewater containing phenolic compounds by electrocoagulation using a fixed bed electrochemicalreactor, Int. J. Electrochem. Sci. 8 (2013) 1534–1550, https://doi.org/10.1016/S1452-3981(23)14117-4.

[37] N.V. Pradeep, S. Anupama, K. Navya, H.N. Shalini, M. Idris, U.S. Hampannavar, Biological removal of phenol from wastewaters: a mini review, Appl. Water Sci. 5 (2015) 105–112, https://doi.org/10.1007/s13201-014-0176-8.

[38] National Pollutant Release Inventory (NPRI) Substance List, (n.d.). https://www.canada.ca/en/environment-climate-change/services/national-pollutant-release-inventory/substances-list.html (accessed February 19, 2023).

[39] Emergency Planning and Community Right to Know Act (EPCRA) Section 313 Chemical list for reporting year 2014, (n.d.). https://www.epa.gov/toxics-release-inventory-tri-program/tri-chemical-list-ry-2014-including-toxic-chemical-categories (accessed February 19, 2023).

[40] M.B. Ahmed, J.L. Zhou, H.H. Ngo, W. Guo, N.S. Thomaidis, J. Xu, Progress in the biological and chemical treatment technologies for emerging contaminant removal from wastewater: a critical review, J. Hazard. Mater. 323 (2017) 274–298, https://doi.org/10.1016/j.jhazmat.2016.04.045.

[41] N. Khan, F. Basheer, I. Farooqi, Treatment of Pulp and paper mill wastewater by column type sequencing batch reactor, J. Ind. Res. Technol. 1 (2011) 12–16.

[42] L.G.C. Villegas, N. Mashhadi, M. Chen, D. Mukherjee, K.E. Taylor, N. Biswas, A short review of techniques for phenol removal from wastewater, Curr. Pollut. Rep. 2 (2016) 157–167, https://doi.org/10.1007/s40726-016-0035-3.

[43] R. Subha, O.A. Sridevi, D. Anitha, D. Sudha, Treatment methods for the removal of phenol from water- A Review. International Conference on Systems, Science, Control, Communication, Engineering and Technology, 2015, pp. 199–203.

[44] N. Horzum, R. Muñoz-Espí, G. Glasser, M.M. Demir, K. Landfester, D. Crespy, Hierarchically structured metal oxide/silica nanofibers by colloid electrospinning, ACS Appl. Mater. Interfaces 4 (2012) 6338–6345, https://doi.org/10.1021/am301969w.

[45] Z. Ma, W. Chen, Z. Hu, X. Pan, M. Peng, G. Dong, S. Zhou, Q. Zhang, Z. Yang, J. Qiu, Luffa-sponge-like glass—TiO2 composite fibers as efficient photocatalysts for environmental remediation, ACS Appl. Mater. Interfaces 5 (15) (2013) 7527–7536, https://doi.org/10.1021/am401827k.

[46] W. Stöber, A. Fink, Controlled growth of monodisperse silica spheres in the micron size range, J. Colloid Interface Sci. 26 (1968) 62–69. https://doi.org/10.1109/ICOSP.2006.345929.

[47] G. Leofanti, M. Padovan, G. Tozzola, B. Venturelli, Surface area and pore texture of catalysts, Catal. Today 41 (1998) 207–219, https://doi.org/10.1016/S0920-5861(98)00050-9.

[48] M. Thommes, K. Kaneko, A.V. Neimark, J.P. Olivier, F. Rodriguez-Reinoso, J. Rouquerol, K.S.W. Sing, Physisorption of gases, with special reference to the evaluation of surface area and pore size distribution (IUPAC technical report), Pure Appl. Chem. 87 (2015) 1051–1069, https://doi.org/10.1515/pac-2014-1117.

[49] D.T. Cromer, K. Herrington, The structures of anatase and rutile, J. Am. Chem. Soc. 77 (1955) 4708–4709, https://doi.org/10.1021/ja01623a004.

[50] B. Ingham, M.F. Toney, 1 - X-ray diffraction for characterizing metallic films, in: K. Barmak, K. Coffey (Eds.), Metallic Films for Electronic, Optical and Magnetic Applications, Woodhead Publishing, 2014, pp. 3–38. https://doi.org/10.1533/9780857096296.1.3.

[51] W. Su, J. Zhang, Z. Feng, T. Chen, P. Ying, C. Li, Surface phases of TiO2 nanoparticles studied by UV Raman spectroscopy and FT-IR spectroscopy, J. Phys. Chem. C 112 (2008) 7710–7716, https://doi.org/10.1021/jp7118422.

[52] I. Djerdj, A.M. Tonejc, Structural investigations of nanocrystalline TiO2 samples, J. Alloys Compd. 413 (2006) 159–174, https://doi.org/10.1016/j.jallcom.2005.02.105.

[53] J.F. Guayaquil-Sosa, B. Serrano-Rosales, P.J. Valadés-Pelayo, H. de Lasa, Photocatalytic hydrogen production using mesoporous TiO_2 doped with Pt, Appl. Catal. B 211 (2017) 337–348, https://doi.org/10.1016/j.apcatb.2017.04.029.

[54] M.-C. Lin, S.-N. Lai, K.T. Le, J.M. Wu, Self-powered photoelectrochemical quartz/TiO2 microsystem through piezopotential sensitized photocatalytic process, Nano Energy 91 (2022), 106640, https://doi.org/10.1016/j.nanoen.2021.106640.

[55] J.S. Piccin, T.R.S.A. Cadaval, L.A.A. de Pinto, G.L. Dotto, Adsorption isotherms in liquid phase: experimental, modeling, and interpretations. Adsorption Processes for Water Treatment and Purification, Springer International Publishing, 2017, pp. 19–51, https://doi.org/10.1007/978-3-319-58136-1_2.

[56] D.L. Liao, G.S. Wu, B.Q. Liao, Zeta potential of shape-controlled TiO_2 nanoparticles with surfactants, Colloids Surf. A 348 (2009) 270–275, https://doi.org/10.1016/j.colsurfa.2009.07.036.

[57] F. Rouquerol, J. Rouquerol, S. Kenneth, G. Mauri, P. Llewellyn, Adsorption by Powders and Porous Solids: Principles, Methodology and Applications, second ed., Academic Press, France, 2012.

[58] Z. Yin, X. Zhang, X. Yuan, W. Wei, Y. Xiao, S. Cao, Constructing TiO_2@Bi_2O_3 multi-heterojunction hollow structure for enhanced visible-light photocatalytic performance, J. Clean. Prod. 375 (2022) 134122, https://doi.org/10.1016/j.jclepro.2022.134112.

[59] X. Xuan Zhang, Y. Guan Xiao, S. Sheng Cao, Z. Liang Yin, Z.Q. Liu, Ternary TiO_2@Bi_2O_3@TiO_2 hollow photocatalyst drives robust visible-light photocatalytic performance and excellent recyclability, J. Clean. Prod. 352 (2022) 131560, https://doi.org/10.1016/j.jclepro.2022.131560.

[60] T.T.T. Dang, S.T.T. Le, D. Channei, W. Khanitchaidecha, A. Nakaruk, Photodegradation mechanisms of phenol in the photocatalytic process, Res. Chem. Intermed. 42 (2016) 5961–5974, https://doi.org/10.1007/s11164-015-2417-3.

[61] F. Bosca, M.L. Marin, O. Cabezuelo, L. Ponce, Fotocatalizador para el tratamiento de fluidos que contengan materia orgánica, P202230020, 2022.